# Simulating the Two-Dimensional *t-J* Model at Finite Doping with Neural Quantum States

Hannah Lange,[1,2,3,*,†] Annika Böhler,[1,2,*,‡] Christopher Roth,[4] and Annabelle Bohrdt[5,2]

[1]*Department of Physics and Arnold Sommerfeld Center for Theoretical Physics (ASC), Ludwig-Maximilians-Universität München, Theresienstraße 37, München D-80333, Germany*

[2]*Munich Center for Quantum Science and Technology, Schellingstraße 4, Munich D-80799, Germany*

[3]*Max-Planck-Institute for Quantum Optics, Hans-Kopfermann-Straße 1, Garching D-85748, Germany*

[4]*Center for Computational Quantum Physics, Flatiron Institute, 162 5th Avenue, New York, New York 10010, USA*

[5]*University of Regensburg, Universitätsstraße 31, Regensburg D-93053, Germany*

(Received 22 January 2025; revised 31 July 2025; accepted 27 August 2025; published 24 September 2025)

Simulating large, strongly interacting fermionic systems remains a major challenge for existing numerical methods. In this Letter, we introduce Gutzwiller projected hidden fermion determinant states (G-HFDS) to simulate the strongly interacting limit of the Fermi-Hubbard model, namely the *t-J* model, across the entire doping regime. We demonstrate that the G-HFDS achieve energies competitive with matrix product states on lattices as large as $10 \times 10$ sites while using several orders of magnitude fewer parameters, suggesting the potential for efficient application to even larger system sizes. This remarkable efficiency enables us to probe low-energy physics across the full doping range, providing new insights into the competition between kinetic and magnetic interactions and the nature of emergent quasiparticles. Starting from the low-doping regime, where magnetic polarons dominate the low energy physics, we track their evolution with increasing doping and different next-nearest neighbor hopping amplitudes through analyses of spin and polaron correlation functions as well as the Fermi surface. Our findings demonstrate the potential of determinant-based neural quantum states with an inherent fermionic sign structure, opening the way for simulating large-scale fermionic systems at any particle filling.

DOI: 10.1103/rc31-5hl9

Understanding the microscopic physics of large, interacting quantum materials such as unconventional superconductors [1] has been a long-standing challenge in theoretical condensed matter physics. A model that is believed to be relevant to many phases observed in cuprate superconductors is the two-dimensional Fermi-Hubbard model, or its high interaction limit, the *t-J* model:

$$\begin{aligned}\mathcal{H}_{t\text{-}J} = &-t\sum_{\langle \mathbf{i},\mathbf{j}\rangle,\sigma} \mathcal{P}_G\left(\hat{c}^{\dagger}_{\mathbf{i},\sigma}\hat{c}_{\mathbf{j},\sigma} + \text{H.c.}\right)\mathcal{P}_G \\ &- t'\sum_{\langle\langle \mathbf{i},\mathbf{j}\rangle\rangle,\sigma} \mathcal{P}_G\left(\hat{c}^{\dagger}_{\mathbf{i},\sigma}\hat{c}_{\mathbf{j},\sigma} + \text{H.c.}\right)\mathcal{P}_G \\ &+ J\sum_{\langle \mathbf{i},\mathbf{j}\rangle}\left(\hat{S}_{\mathbf{i}}\cdot\hat{S}_{\mathbf{j}} - \frac{1}{4}\hat{n}_{\mathbf{i}}\hat{n}_{\mathbf{j}}\right), \qquad (1)\end{aligned}$$

with the fermionic annihilation (creation) operators $\hat{c}^{(\dagger)}_{\mathbf{i},\sigma}$ at site $\mathbf{i}$ with spin $\sigma$, spin operators $\hat{\mathbf{S}}_{\mathbf{i}} = \sum_{\sigma,\sigma'} \hat{c}^{\dagger}_{\mathbf{i},\sigma}(\boldsymbol{\sigma}_{\sigma\sigma'}/2)\hat{c}_{\mathbf{i},\sigma'}$ and density operators $\hat{n}_{\mathbf{i}}$. Furthermore, $\mathcal{P}_G$ projects out states with more than one particle per site. At half filling, the system realizes an antiferromagnetic (AFM) Mott insulator. The competition between kinetic (next-) nearest neighbor hopping amplitude $t^{(\prime)}$ and antiferromagnetic energy scale $J$ leads to the formation of magnetic polarons, i.e., heavily dressed dopants [2–6], at low hole doping, and is believed to give rise to the pseudogap, superconductivity, and stripe order upon further doping [7–9]. Finally, the system becomes a Fermi liquid at high hole doping [10]. The extent of these phases depends on the type of dopants, where hole and particle dopings are modeled by different signs of $t'$.

Despite its seeming simplicity, simulating the Fermi-Hubbard or the *t-J* model, particularly at finite hole doping, has proven to be highly challenging, even with impressive numerical studies [11–14] and recent advances on quantum simulation platforms [15]. While variational methods like matrix product states (MPS) [16] become prohibitively expensive when applied to large two-dimensional systems, other established techniques like quantum Monte Carlo (QMC) [17] face the sign problem at finite doping, which can be overcome by auxiliary field QMC with the cost of introducing a bias [13]. Neural quantum states (NQS)

*These authors contributed equally to this work.

†Contact author: hannah.lange@physik.uni-muenchen.de

‡Contact author: annika.boehler@physik.uni-muenchen.de

*Published by the American Physical Society under the terms of the Creative Commons Attribution 4.0 International license. Further distribution of this work must maintain attribution to the author(s) and the published article's title, journal citation, and DOI.*

introduced by Carleo and Troyer [18] can potentially overcome some of these limitations: NQS have demonstrated the ability to capture states with volume-law entanglement [19–23] and have been shown to outperform traditional methods like MPS in two-dimensional spin systems [24–28]. While early research predominantly focused on spin-1/2 systems, recent efforts have increasingly turned to the simulation of bosonic and fermionic systems [29–31].

Here, we employ a neural network approach to simulate the two-dimensional $t$-$J$ model, namely Gutwiller projected *hidden fermion determinant states* (G-HFDS). We show that relative to MPS wavefunctions, the G-HFDS are extremely efficient, particularly at intermediate doping. Specifically, G-HFDS can achieve the same energies as MPS, using only a very small fraction of the parameters. As a consequence of this efficiency, we are able to study the physical properties of the $t$-$J$ model in a full doping scan. We calculate spin-spin and polaron correlations, compare them to experimental observations [32,33], and track their evolution with different next-nearest neighbor hopping amplitudes, corresponding to hole and particle doping. Furthermore, G-HFDS allow for periodic boundary conditions, enabling the evaluation of momentum resolved quantities. Specifically we analyze the momentum resolved density—a quantity that is considered highly informative, especially in the context of the pseudogap phase but hardly accessible in this regime using methods like MPS.

*Neural network architecture*—We introduce G-HFDS, combining the HFDS [34] and the concept of Gutzwiller projected wave functions [35–38]. For a sampled set of Fock space configurations $\{\boldsymbol{\sigma}\}$, we approximate

$$|\Psi\rangle \approx \sum_{\{\boldsymbol{\sigma}\}} \psi_{\mathrm{G-HFDS}}(\sigma)|\sigma\rangle, \tag{2}$$

with $\psi_{\mathrm{G-HFDS}}(\boldsymbol{\sigma}) = \mathcal{P}_G \psi(\boldsymbol{\sigma})$. The former is based on a Slater determinant of both physical and auxiliary *hidden* fermions, similar to Jastrow-factors [39] and neural backflow transformations [40–45]; see Supplemental Material (SM) [46] including Refs. [47–57]. The latter introduces a significant amount of correlations by restricting the sampling to configurations with at maximum singly occupied sites, effectively applying the projector $\hat{\mathcal{P}}_G$. Note that there is no additional computational cost in order to apply this projection, making G-HFDS an appealing candidate for simulating the $t$-$J$ model but also spin models, the Kugel-Khomskii, or any model with a projection of this form. Furthermore, it allows for starting the optimization from a pure Gutzwiller wave function by initializing the physical fermions accordingly.

The trainable upper matrix and the Feed forward neural network (FFNN) representing the lower matrix are then optimized using variational Monte Carlo [17,58] to approximate an imaginary time evolution using the variant of stochastic reconfiguration introduced in Ref. [24]. We additionally enforce a global spin flip symmetry.

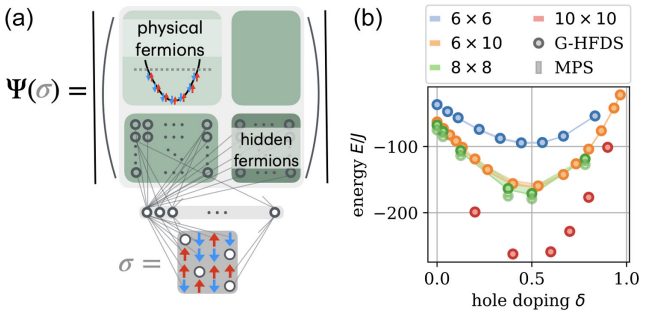



FIG. 1. (a) Hidden fermion determinant states (HFDS). The wave function coefficients $\psi(\sigma)$ in the Fock basis $\sigma$ are parameterized as a determinant of physical and ancilla (*hidden*) orbitals. The orbitals of the latter are configuration dependent, with the dependence learned by a feedforward neural network. (b) Energies for the $t$-$J$ model on open boundary $6 \times 6$ (blue), $6 \times 10$ (orange), $8 \times 8$ (green), and $10 \times 10$ (red) lattices at $t/J = 3$ and different hole doping $\delta$, obtained from MPS (shaded regions for energies obtained with bond dimensions $\chi = 128, \ldots, 2048$) and the G-HFDS (markers). Light green markers represent $8 \times 8$ energies for periodic boundaries in both directions from the G-HFDS. Error bars denoting the error of the mean are smaller than the markers.

For the HFDS, the augmentation of the physical Hilbert space leads to an enlarged Slater determinant $\psi(\boldsymbol{\sigma})$ consisting of four blocks; see Fig. 1(a). The upper left (lower right) block represents the single particle orbitals of the physical (hidden) fermions. Respectively, the off-diagonal blocks represent interactions between the physical and auxiliary states. Hereby, the upper (lower) part of the matrix is parameterized by a set of trainable real-valued parameters [by a (configuration dependent) feedforward neural network] [34]. We start by initializing the physical block with free fermion orbitals and setting the hidden block (off-diagonal blocks) to identity (zero), resulting in the well-known variational ansatz for $t$-$J$ systems of Gutzwiller projected wave functions [35–38].

*Comparison with MPS*—The energies for the $t$-$J$ model are shown in Fig. 1(b) for $8 \times 8$ ($6 \times 10$, $6 \times 6$) lattices at different hole dopings $\delta$. All calculations are done for $t/J = 3.0$ and $t' = 0$ unless stated differently. For comparison with MPS, open boundary systems are mainly considered. Note that, in contrast to MPS, HFDS can be used with open, cylindrical, and periodic boundary conditions in both directions without any difference in computational cost. As an example, we show the HFDS energies for a $8 \times 8$ torus. We compare the open boundary results from the G-HFDS represented by the circles using a FFNN with a single hidden layer with 128 (128, 78) nodes and 20 hidden fermions to $U(1) \times SU(2)$ symmetric matrix product calculations with bond dimensions $\chi = 128, \ldots, 2048$, corresponding to up to $\approx$6000 $U(1)$ states, which are represented by the shaded regions. In all

cases, the results from G-HFDS and the MPS calculations with the highest bond dimension agree very well. We additionally calculate the ground state energies of a $10 \times 10$ system with G-HFDS, which is extremely challenging for MPS methods.

Note that for intermediate dopings, the MPS energies for the large system strongly change between $\chi = 128, \ldots, 2048$ (shown by the shaded region), indicating that in this highly complicated regime with different competing energy scales $t$ and $J$ these bond dimensions are not sufficient for ensure convergence. In this regime, the power of G-HFDS states unfolds, as shown in more detail for $8 \times 8$ systems at exemplary $\delta$ in Fig. 2. On the right side of Fig. 2, the energy over the number of parameters used by the MPS is shown, estimated as $P_{\mathrm{MPS}} = d\chi^2 L_x L_y$, with $d = 3$ being the local dimension. At low and high doping, the MPS calculations converge for $\chi > 512$ $SU(2)$ states, but for intermediate doping the energy significantly decreases up to the highest bond dimension $\chi = 2048$ used here. We choose this as the maximal bond dimension in order to have a comparable number of G-HFDS parameters $P_{\mathrm{HFDS}}$ and MPS parameters $P_{\mathrm{MPS}}$. For the G-HFDS we choose to vary $P_{\mathrm{HFDS}}(\delta) \propto N_h^2$ at a fixed doping $\delta$ by changing the number of hidden fermions $N_h$. In all cases, the energies obtained with the G-HFDS (see Fig. 2, left) agree well with the MPS energies but require more than two orders of magnitude less parameters.

Focusing on the highest considered $P_{\mathrm{HFDS}}$ for each $\delta$, we calculate the $P_{\mathrm{MPS}}$ that is needed to obtain the same energy by fitting the MPS energies to a logarithmic dependence and determining the intersection of the fit

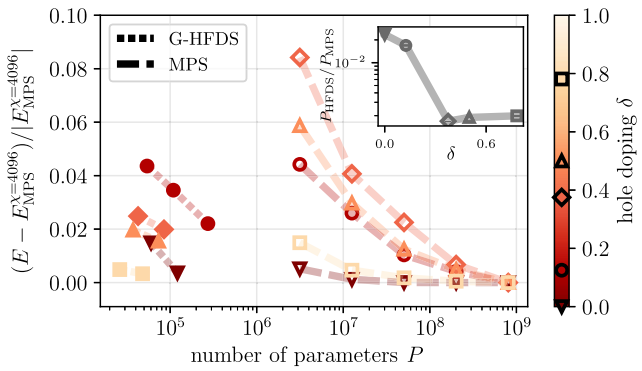



FIG. 2. Comparison of energies obtained from the G-HFDS (filled markers, dotted lines) and MPS (empty markers, dashed lines) for a $8 \times 8$ lattice with open boundaries at exemplary dopings $\delta$ indicated by the color bar. For the G-HFDS (MPS), the number of parameters $P_{\mathrm{HFDS}}$ ($P_{\mathrm{MPS}}$) is varied by the number of hidden fermions $N_h$ (bond dimension $\chi$). For the G-HFDS, error bars denoting the error of the mean are smaller than the markers. For error estimates of the MPS results, see SM [46]. Inset: for each $\delta$, the number of parameters $P_{\mathrm{HFDS}}(\delta) \propto N_h$ for the highest considered $N_h$ is compared to the $P_{\mathrm{MPS}}$ needed to obtain the same energy. The fraction $P_{\mathrm{HFDS}}/P_{\mathrm{MPS}}$ indicates the efficiency of the G-HFDS representation.

with a horizontal line through the G-HFDS energies. The fraction $P_{\mathrm{HFDS}}/P_{\mathrm{MPS}}$ is shown in the inset. Again, it can be seen that the G-HFDS are particularly efficient in the intermediate doping regime. Furthermore, the training of the G-HFDS on GPUs with up to 1500 steps took 6 to 15 GPU h, while the MPS calculations ran several days on a CPU.

*Full doping scans*—In order to investigate the evolution of the interplay between magnetic and kinetic degrees of freedom with doping, e.g., the extent of the polaron regime, full doping scans of low energy state physical observables like correlation functions are needed. However, while at a finite temperature, spin and polaron correlation functions have been measured; e.g., on quantum simulation platforms realizing the Hubbard model [32,33], accessing low energy or ground state observables in the full doping regime has remained experimentally challenging and computationally expensive, particularly at finite dopings. With the efficiency of our G-HFDS ansatz in the intermediate doping regime, such doping scans become feasible. In the following, we compare our low energy two-point spin and three-point polaron correlations to experimental measurements at finite temperature and make predictions for experimentally feasible five-point polaron correlations. In all cases, we take averages over the full system, excluding terms at the boundaries where the expectation values would involve sites outside the samples.

We start by analyzing the connected spin-spin correlation function between spins at sites $\boldsymbol{r}_1$ and $\boldsymbol{r}_2$,

$$C(\mathbf{d}) = \frac{1}{N_d} \sum_{\substack{\mathbf{r}_1,\mathbf{r}_2 \text{ s.t.} \\ \mathbf{r}_1 - \mathbf{r}_2 = \mathbf{d}}} \eta_{\mathbf{r}_1\mathbf{r}_2} \langle \hat{S}^z_{\mathbf{r}_1} \hat{S}^z_{\mathbf{r}_2} \rangle_c, \tag{3}$$

where $N_d$ is the number of terms in the sum, $\eta_{\mathbf{r}_1\mathbf{r}_2} = [\sigma(\hat{S}^z_{\mathbf{r}_1})\sigma(\hat{S}^z_{\mathbf{r}_2})]^{-1}$, a normalization accounting for the increased presence of holes at higher doping levels (with the standard deviation $\sigma$), and $\langle \ldots \rangle_c$ denotes the connected correlator with lower-order terms subtracted, as defined in SM [46]. The results for different values of $d$ are displayed in Fig. 3 and compared to MPS results ($T = 0$) and experimental measurements from Ref. [32], taken at temperature $k_B T = 0.4t$ in the Fermi-Hubbard model. Similar measurements were also taken in Ref. [33]. The results for MPS and G-HFDS agree very well: at half-filling, $d = (1, 0)$ reveals a clear antiferromagnetic alignment of spins, while we observe ferromagnetic correlations at $d = (1, 1)$. Upon doping, both correlations become weaker. We see the same behavior for spins at larger distances $d = (2, 0), (2, 1)$, consistent with AFM Néel order at half-filling, which quickly decreases with higher doping.

At doping of $\delta \approx 0.25$, some correlations undergo a sign change. This sign change is associated with a breakdown of the magnetic polaron regime and a crossover to a Fermi

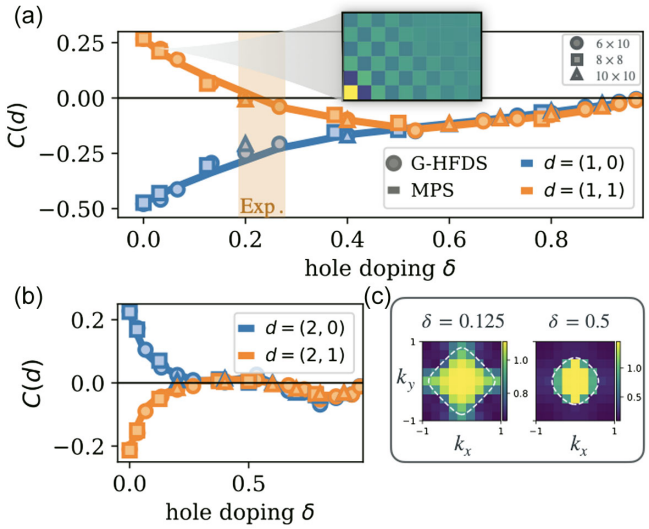



FIG. 3. (a),(b) Two-point spin-spin correlators $C(\mathbf{d})$ for different distances $\mathbf{d}$ in the $6 \times 10$ (circles), $8 \times 8$ (squares), $10 \times 10$ (triangles) lattice with open boundaries from the optimized G-HFDS. Lines represent results from MPS on $6 \times 10$ systems. The sign change region from the experiment, Ref. [32], is denoted by the orange region for $d = (1, 1)$. Inset: full spin correlation map for two holes and a reference spin in the lower left corner; color bar limits are $-0.25$ (blue) to 0.25 (yellow). Error bars denoting the error of the mean are smaller than the markers. (c) $k$-space densities $n_{\mathbf{k}} = n_{\mathbf{k}\uparrow} + n_{\mathbf{k}\downarrow}$ for exemplary dopings before and after the sign crossing. White dashed lines indicate the analytical result for the Fermi surface of free spin-1/2 fermions.

liquid and is also observed in the experiment (shaded region) [32]. The crossover is further associated with a qualitative change in the Fermi surface (FS): in the low-doping regime, the charge carriers are free magnetic polarons, associated with a small FS and hole pockets, while the Fermi liquid has a large FS of free fermions. We analyze the Fermi surface from the occupation in $k$-space given as $\langle n_{\mathbf{k}\sigma}\rangle = (1/L^2)\sum_{j,j'} e^{i\mathbf{k}(j-j')}\langle c^\dagger_{j\sigma} c_{j'\sigma}\rangle$; the results are shown in Fig. 3(c). For dopings above the sign change $\delta > 0.25$, we find a FS closely aligned with free fermions, while for $\delta < 0.25$ before the sign change, we find a qualitative change, where the distribution is shifted toward $(\pm\pi, 0)$ and $(0, \pm\pi)$ compared to the free fermion FS. The sign change can also be understood in terms of the geometric string theory [6,15,59], where motion of a single dopant in a magnetic background creates a string $\Sigma$ of displaced spins; see Fig. 4(a). Beyond a single dopant, this description is still valid in the low doping regime [60], but with an increasing number of dopants, strings—and hence also the corresponding correlations—start to mix. Once a certain level of mixing is reached, this introduces a sign change in some correlations. Note that the full correlation map does not show any signature of a stripe phase in the low doping regime (see inset of Fig. 3) as, e.g., discussed in Refs. [9,61,62]. This is different for cylindrical boundaries; see SM [46].

The extent of the magnetic polaron regime can be studied in more detail by considering correlations of two spins around a hole (see also Ref. [15]):

$$C_\circ(\mathbf{d}, \mathbf{r}_h) = \frac{1}{N_d N_{r_h}} \sum_{\mathbf{r}_h} \sum_{\substack{\mathbf{r}_1, \mathbf{r}_2 \text{ s.t.} \\ \mathbf{r}_1 - \mathbf{r}_2 = \mathbf{d} \\ |\mathbf{r}_1 - \mathbf{r}_h| = 1}} \tilde{\eta} \langle \hat{S}^z_{\mathbf{r}_1} \hat{S}^z_{\mathbf{r}_2} \hat{n}^h_{\mathbf{r}_h} \rangle_c, \qquad (4)$$

with the hole density $\hat{n}^h_{\mathbf{r}_h}$ and $\tilde{\eta} = [\langle \hat{n}^h_{\mathbf{r}_h}\rangle \sigma(\hat{S}^z_{\mathbf{r}_1}) \sigma(\hat{S}^z_{\mathbf{r}_2})]^{-1}$, measuring the influence of the hole on the spin correlations

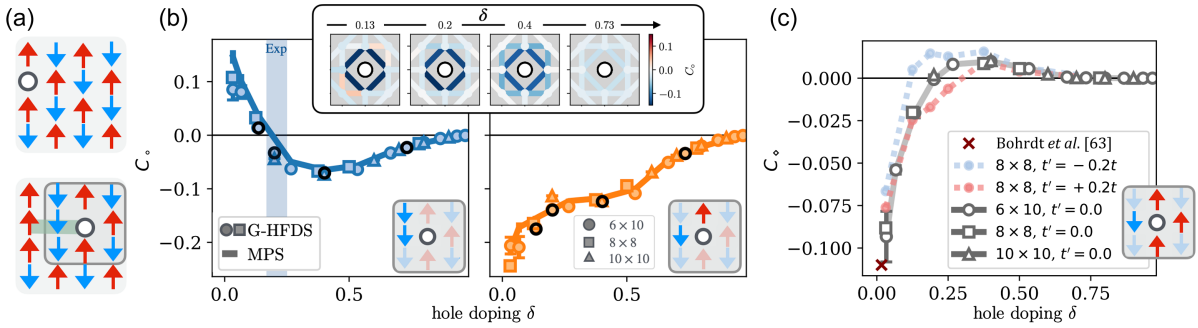



FIG. 4. Investigating the polaron regime. (a) Geometric string theory: when the hole (represented by the circle) moves away from its original position (top), it distorts the magnetic background (blue and red arrows), giving rise to an energy cost that increases linearly with the distance; a *string* (green) of length $l_\Sigma$. (b) Three-point polaron correlators $C_\circ(\mathbf{d}, \mathbf{r}_h)$ for $6 \times 10$ (circles), $8 \times 8$ (squares), and $10 \times 10$ (triangles) systems with open boundaries and different distances $\mathbf{d} = (0, 1), (1, 1)$ (left, right). Circles represent data obtained from the optimized NQS wavefunction, lines $6 \times 10$ MPS calculations. The sign change region from the experiment Ref. [32] is denoted by the blue region for $d = (1, 0)$. Black markers indicate the doping values for which the full correlation map for the $6 \times 10$ lattice is shown in the inset. (c) Five-point polaron correlations $C_\diamond$ for $6 \times 10$, $8 \times 8$, and $10 \times 10$ systems with open boundaries for different next-nearest neighbor hoppings $t'$. For a single hole, we compare to the result from Ref. [63]. Error bars (mostly smaller than the markers) show the error of the mean. The position of the hole relative to the spins $\mathbf{r}_h$ is shown in the insets for (b) and (c). In the very low doping regime, positions with $\langle \hat{n}_{\mathbf{r}} \rangle = 0$ exist, leading to effectively larger errors of both $C_\circ$ and $C_\diamond$. These errors are estimated by two different realizations of the G-HFDS; see the main text.

in its vicinity. The results from G-HFDS, MPS, and experiment [32] are shown in Fig. 4(b). For low doping, the antiferromagnetic background is perturbed by the hole as schematically illustrated in Fig. 4(a), i.e., nearest neighbor $[d = (1,0)]$ spins align more ferromagnetically and diagonal neighbors $[d = (1,1)]$ align more antiferromagnetically. At low doping, the absolute strength of magnetic correlations decreases due to the presence of holes as observed before. Note that Eq. (4) is not well defined if $\langle \hat{n}^h_{\mathbf{r}_h} \rangle = 0$. In these cases, we set the contribution of the respective term to the sum to zero. For the very low hole dopings where this problem occurs for the $6 \times 10$ systems (marked by the gray area), we encounter higher error bars, estimated by the results from two different parameterizations of the state. All other error bars indicate the sampling error.

Furthermore, again a sign change in the correlations with $d = (1,0)$ occurs, indicating a transition from the strongly correlated state described by magnetic string theory to a Fermi Liquid, where the Pauli exclusion principle leads to enhanced antiferromagnetic alignment [64]. For cuprate materials, the same qualitative change of observables takes place at a similar doping level [10]. Note that the presence of real space pairs would lead to similar signatures as observed here for the polaron correlations [61].

To further investigate the nature of the polaron, the five-point correlator,

$$C_\diamond = \frac{2^4}{N_r} \sum_{\mathbf{r}_h} \frac{1}{\langle \hat{n}^h_{\mathbf{r}_\mathbf{h}} \rangle} \left\langle \hat{n}^h_{\mathbf{r}_\mathbf{h}} \hat{S}^z_{\mathbf{r}_\mathbf{h}+\hat{e}_x} \hat{S}^z_{\mathbf{r}_\mathbf{h}-\hat{e}_x} \hat{S}^z_{\mathbf{r}_\mathbf{h}+\hat{e}_y} \hat{S}^z_{\mathbf{r}_\mathbf{h}-\hat{e}_y} \right\rangle, \quad (5)$$

is considered [63] in Fig. 4(c). At very low doping, $C_\diamond$ depends on the probability of configurations with string lengths $l_\Sigma = 0$ and $l_\Sigma > 0$. As schematically shown in Fig. 4(a), $C_\diamond > 0$ for $l_\Sigma = 0$, while for $l_\Sigma > 0$, $C_\diamond < 0$. The fact that at low doping we find $C_\diamond < 0$ indicates that configurations with $l_\Sigma > 0$ are more likely, in agreement with Ref. [65]. Upon increasing the doping, $C_\diamond$ become positive with the sign change depending on the next-nearest neighbor hopping amplitude $t'$. This is in agreement with the faster decay of AFM correlations with respect to doping for hole ($t' < 0$) vs particle ($t' > 0$) doping [10].

*Conclusion*—In this Letter, we demonstrate that Gutzwiller projected hidden fermion determinant states (G-HFDS) effectively capture the low-energy states of the $t$-$J$ model. In particular, we show that G-HFDS can encode energies comparable to those obtained from matrix product state (MPS) calculations with 2048 $U(1) \times SU(2)$ symmetric states across the full doping regime, while utilizing up to four orders of magnitude fewer parameters. Furthermore, they can be used with periodic boundary conditions. This parameter efficiency positions G-HFDS as a competitive alternative to MPS, particularly as GPU resources continue to advance.

In addition to improving training speed, reducing parameter count makes it easier to save model weights as they take up far less memory. As a result, we are able to share model weights across the full doping scan so that others can access the trained models. The model weights can be used either to compute new correlation functions or as a starting point for simulating closely related models.

Our analysis reveals that G-HFDS excel in the challenging intermediate doping regime, facilitating the exploration of low-energy observables throughout the entire doping scan. Specifically, we investigate spin and polaron correlations, comparing our findings with experimental data and MPS calculations. The doping dependence of these correlation functions and the critical dopings at which their signs change align well with existing literature. This Letter paves the way for further investigations of correlated systems across the full doping range and low temperatures.

Our implementation of hidden fermions is adapted from the neural backflow [66] and is available at [67], where the trained models can also be found.

*Acknowledgments*—We thank Fabian Grusdt, Tizian Blatz, Timothy Harris, and Subir Sachdev for useful discussions. All DMRG calculations were performed using the SyTen toolkit [68,69] developed and maintained by C. Hubig, F. Lachenmaier, N.-O. Linden, T. Reinhard, L. Stenzel, A. Swoboda, M. Grundner, S. Mardazad, F. Pauw, and S. Paeckel. Information is available at [68] and in SM [46]. A. B., A. B., and H. L. acknowledge the support of the Deutsche Forschungsgemeinschaft (DFG, German Research Foundation) under Germany's Excellence Strategy—EXC-2111–390814868. H. L. acknowledges support by the International Max Planck Research School for Quantum Science and Technology (IMPRS-QST). C. R. acknowledges support from the Flatiron Institute. The Flatiron Institute is a division of the Simons Foundation. NQS simulations were performed using NetKet [70].

*Data availability*—The data that support the findings of this article are openly available [67].

[1] J. G. Bednorz and K. A. Müller, Z. Phys. B **64**, 189 (1986).
[2] L. Bulaevski, É. Nagaev, and D. Khomskii, J. Exp. Theor. Phys. **27**, 836 (1968).
[3] W. F. Brinkman and T. M. Rice, Phys. Rev. B **2**, 1324 (1970).
[4] S. Sachdev, Phys. Rev. B **39**, 12232 (1989).
[5] C. L. Kane, P. A. Lee, and N. Read, Phys. Rev. B **39**, 6880 (1989).
[6] F. Grusdt, M. Kánasz-Nagy, A. Bohrdt, C. S. Chiu, G. Ji, M. Greiner, D. Greif, and E. Demler, Phys. Rev. X **8**, 011046 (2018).
[7] S. M. O'Mahony, W. Ren, W. Chen, Y. X. Chong, X. Liu, H. Eisaki, S. Uchida, M. H. Hamidian, and J. C. S. Davis, Proc. Natl. Acad. Sci. U.S.A. **119**, e2207449119 (2022).

[8] S. Badoux, W. Tabis, F. Laliberté, G. Grissonnanche, B. Vignolle, D. Vignolles, J. Béard, D. A. Bonn, W. N. Hardy, R. Liang, N. Doiron-Leyraud, L. Taillefer, and C. Proust, Nature (London) **531**, 210 (2016).

[9] S. Jiang, D. J. Scalapino, and S. R. White, Proc. Natl. Acad. Sci. U.S.A. **118**, e2109978118 (2021).

[10] B. Keimer, S. A. Kivelson, M. R. Norman, S. Uchida, and J. Zaanen, Nature (London) **518**, 179 (2015).

[11] M. Qin, C.-M. Chung, H. Shi, E. Vitali, C. Hubig, U. Schollwöck, S. R. White, and S. Zhang (Simons Collaboration on the Many-Electron Problem), Phys. Rev. X **10**, 031016 (2020).

[12] T. Schäfer, N. Wentzell, F. Šimkovic, Y.-Y. He, C. Hille, M. Klett, C. J. Eckhardt, B. Arzhang *et al.*, Phys. Rev. X **11**, 011058 (2021).

[13] H. Xu, C.-M. Chung, M. Qin, U. Schollwöck, S. R. White, and S. Zhang, Science **384**, eadh7691 (2024).

[14] D. P. Arovas, E. Berg, S. A. Kivelson, and S. Raghu, Annu. Rev. Condens. Matter Phys. **13**, 239 (2022).

[15] A. Bohrdt, L. Homeier, C. Reinmoser, E. Demler, and F. Grusdt, Ann. Phys. (N.Y.) **435**, 168651 (2021).

[16] U. Schollwöck, Ann. Phys. (N.Y.) **326**, 96 (2011).

[17] F. Becca and S. Sorella, *Quantum Monte Carlo Approaches for Correlated Systems* (Cambridge University Press, Cambridge, England, 2017).

[18] G. Carleo and M. Troyer, Science **355**, 602 (2017).

[19] O. Sharir, A. Shashua, and G. Carleo, Phys. Rev. B **106**, 205136 (2022).

[20] D.-L. Deng, X. Li, and S. Das Sarma, Phys. Rev. X **7**, 021021 (2017).

[21] X. Gao and L.-M. Duan, Nat. Commun. **8**, 662 (2017).

[22] Z. Denis, A. Sinibaldi, and G. Carleo, Phys. Rev. Lett. **134**, 079701 (2025).

[23] Y. Levine, O. Sharir, N. Cohen, and A. Shashua, Phys. Rev. Lett. **122**, 065301 (2019).

[24] R. Rende, L. L. Viteritti, L. Bardone, F. Becca, and S. Goldt, Commun. Phys. **7**, 260 (2024).

[25] A. Chen and M. Heyl, Nat. Phys. **20**, 1476 (2024).

[26] M. Reh, M. Schmitt, and M. Gärttner, Phys. Rev. B **107**, 195115 (2023).

[27] J.-Q. Wang, H.-Q. Wu, R.-Q. He, and Z.-Y. Lu, Phys. Rev. B **109**, 245120 (2024).

[28] C. Roth, A. Szabó, and A. H. MacDonald, Phys. Rev. B **108**, 054410 (2023).

[29] H. Lange, A. V. de Walle, A. Abedinnia, and A. Bohrdt, Quantum Sci. Technol. **9**, 040501 (2024).

[30] M. Medvidović and J. R. Moreno, Eur. Phys. J. Plus **139**, 631 (2024).

[31] Y. Nomura and M. Imada, J. Phys. Soc. Jpn. **94**, 031001 (2025).

[32] J. Koepsell, D. Bourgund, P. Sompet, S. Hirthe, A. Bohrdt, Y. Wang, F. Grusdt, E. Demler, G. Salomon, C. Gross, and I. Bloch, Science **374**, 82 (2021).

[33] L. W. Cheuk, M. A. Nichols, K. R. Lawrence, M. Okan, H. Zhang, E. Khatami, N. Trivedi, T. Paiva, M. Rigol, and M. W. Zwierlein, Science **353**, 1260 (2016).

[34] J. R. Moreno, G. Carleo, A. Georges, and J. Stokes, Proc. Natl. Acad. Sci. U.S.A. **119**, e2122059119 (2022).

[35] C. Gros, Ann. Phys. (N.Y.) **189**, 53 (1989).

[36] J. B. Marston and I. Affleck, Phys. Rev. B **39**, 11538 (1989).

[37] B. Dalla Piazza, M. Mourigal, N. B. Christensen, G. J. Nilsen, P. Tregenna-Piggott, T. G. Perring, M. Enderle, D. F. McMorrow, D. A. Ivanov, and H. M. Rønnow, Nat. Phys. **11**, 62 (2015).

[38] B. Dalla Piazza, Theories of Experimentally Observed Excitation Spectra of Square Lattice Antiferromagnets, Ph.D. thesis, EPFL, Lausanne, 2014.

[39] R. Jastrow, Phys. Rev. **98**, 1479 (1955).

[40] R. P. Feynman and M. Cohen, Phys. Rev. **102**, 1189 (1956).

[41] D. Luo and B. K. Clark, Phys. Rev. Lett. **122**, 226401 (2019).

[42] J. Hermann, Z. Schätzle, and F. Noé, Nat. Chem. **12**, 1755 (2020).

[43] D. Pfau, J. S. Spencer, A. G. D. G. Matthews, and W. M. C. Foulkes, Phys. Rev. Res. **2**, 033429 (2020).

[44] J. Kim, G. Pescia, B. Fore, J. Nys, G. Carleo, S. Gandolfi, M. Hjorth-Jensen, and A. Lovato, arXiv:2305.08831.

[45] I. Romero, J. Nys, and G. Carleo, Commun. Phys. **8**, 46 (2025).

[46] See Supplemental Material at http://link.aps.org/supplemental/10.1103/rc31-5hl9 for a more detailed discussion of different neural quantum state architectures for fermions, as well as more details on the matrix product state calculations and definitions of correlation functions.

[47] J. C. Slater, Phys. Rev. **34**, 1293 (1929).

[48] J. Stokes, J. R. Moreno, E. A. Pnevmatikakis, and G. Carleo, Phys. Rev. B **102**, 205122 (2020).

[49] Y. Nomura, A. S. Darmawan, Y. Yamaji, and M. Imada, Phys. Rev. B **96**, 205152 (2017).

[50] S. Humeniuk, Y. Wan, and L. Wang, SciPost Phys. **14**, 171 (2023).

[51] C. Gauvin-Ndiaye, J. Tindall, J. R. Moreno, and A. Georges, arXiv:2311.05749.

[52] Z. Liu and B. K. Clark, Phys. Rev. B **110**, 115124 (2024).

[53] B. J. Wurst, D. M. Kennes, and J. B. Profe, Phys. Rev. Res. **7**, 023316 (2025).

[54] T. D. Barrett, A. Malyshev, and A. I. Lvovsky, Nat. Mach. Intell. **4**, 351 (2022).

[55] K. Inui, Y. Kato, and Y. Motome, Phys. Rev. Res. **3**, 043126 (2021).

[56] H. Lange, F. Döschl, J. Carrasquilla, and A. Bohrdt, Commun. Phys. **7**, 187 (2024).

[57] N. Yoshioka and R. Hamazaki, Phys. Rev. B **99**, 214306 (2019).

[58] I. Goodfellow, Y. Bengio, and A. Courville, *Deep Learning* (MIT Press, Cambridge, MA, 2016).

[59] P. Béran, D. Poilblanc, and R. B. Laughlin, Nucl. Phys. **B473**, 707 (1996).

[60] C. S. Chiu, G. Ji, A. Bohrdt, M. Xu, M. Knap, E. Demler, F. Grusdt, M. Greiner, and D. Greif, Science **365**, 251 (2019).

[61] S. R. White and D. J. Scalapino, Phys. Rev. B **55**, 6504 (1997).

[62] S. R. White and D. J. Scalapino, Phys. Rev. B **60**, R753 (1999).

[63] A. Bohrdt, Y. Wang, J. Koepsell, M. Kánasz-Nagy, E. Demler, and F. Grusdt, Phys. Rev. Lett. **126**, 026401 (2021).

[64] T. Hartke, B. Oreg, N. Jia, and M. Zwierlein, Phys. Rev. Lett. **125**, 113601 (2020).
[65] F. Grusdt, A. Bohrdt, and E. Demler, Phys. Rev. B **99**, 224422 (2019).
[66] G. Carleo, Lattice fermions, from slater determinants to neural backflow transformations, https://netket.readthedocs.io/en/latest/tutorials/lattice-fermions.html.
[67] H. Lange, A. Böhler, C. Roth, and A. Bohrdt, Github repository: Hfdsfortj—simulating the *t-j* model with hidden fermion determinant states, https://github.com/HannahLange/HFDSfortJ.
[68] C. Hubig, F. Lachenmaier, N.-O. Linden, T. Reinhard, L. Stenzel, A. Swoboda, and M. Grundner, The SyTen toolkit, https://syten.eu.
[69] C. Hubig, Symmetry-protected tensor networks, https://edoc.ub.uni-muenchen.de/21348/ (2017).
[70] F. Vicentini, D. Hofmann, A. Szabó, D. Wu, C. Roth, C. Giuliani, G. Pescia, J. Nys, V. Vargas-Calderón, N. Astrakhantsev, and G. Carleo, NETKET3: Machine Learning Toolbox for Many-Body Quantum Systems, SciPost Phys. Codebases 7 (2022).